Surfaces and Interfaces 51 (2024) 104740

Contents lists available at ScienceDirect

Surfaces and Interfaces

journal homepage: www.sciencedirect.com/journal/surfaces-and-interfaces

Understanding interfacial dynamics: Hydrostatic pressure-induced sono-dispersion of carbon nanotubes

Lei Yu [a], Yibiao Lin [a,b], Lianxia Li [c], Hu Zong [a,b], Ying Zhou [b], Su Zhao [a,*], Zhiguo Zhang [d], Nicole Grobert [e], Barbara M Maciejewska [e,*], Ling Qin [f,*]

[a] Ningbo Institute of Industrial Technology Chinese Academy of Sciences, Ningbo, 315201, China
[b] College of Chemical Engineering, Zhejiang University of Technology, Hangzhou, 310014, China
[c] Departments of Mathematics, University of North Carolina at Chapel Hill, NC, 27514, US
[d] Institute of Advanced Wear & Corrosion Resistant and Functional Materials, Jinan University, Guangzhou, 510632, China
[e] Department of Materials, University of Oxford, Oxford, OX1 3 PH, UK
[f] Center of Innovation for Flow through Porous Media, Department of Petroleum Engineering, University of Wyoming, Laramie, WY 82071, US

ARTICLE INFO

Keywords:
Carbon nanotubes
Ultrasonic dispersion
Hydrostatic pressures
Numerical simulation
Nanobubbles
Interfacial dynamics

ABSTRACT

Homogeneously dispersing carbon nanotubes (CNTs) is crucial for minimizing agglomeration issues commonly encountered in commercially available CNTs samples, thereby enhancing their unique mechanical, electrical, thermal, and optical properties. In this study, we propose an alternative hydrostatic pressure-driven dispersion approach to effectively disperse CNTs and assess the impact of hydrostatic pressure on CNTs dispersion in deionized water (DIW). Our results demonstrate that ultrasonic treatment under a hydrostatic pressure of 0.1 MPa enables the achievement of a high concentration of multi-walled carbon nanotubes (MWCNTs) at approximately 4.23 mg/ml, significantly surpassing concentrations reported in recent studies (~1.9 mg/ml). Thin buckypaper generated from these solutions exhibit exceptional electrical conductivity (~4938 S/m). Numerical modeling demonstrates that the shock wave induced by bubble implosion is significantly enhanced, reaching 80 MPa under hydrostatic pressure, markedly higher than atmospheric pressure in previous studies (~1.6 MPa). This enhancement leads to a twofold improvement in dispersion efficiency. For the first time, we reveal the underlying mechanism of nanobubbles (NBs) in dispersion stability. Our experimental results show a significant increase in the generation of NBs resulting from ultrasonic bubble collapse under hydrostatic pressure. This phenomenon plays a crucial role in the long-term stabilization of dispersion, which we observed over several months. The presence of negatively charged hydroxyl groups on the interface of the NBs is identified as a key factor in this stabilization process. The hydrostatic pressure-driven dispersion approach presented is essential for the large-scale dispersion of CNTs and other nanomaterials.

1. Introduction

Carbon nanotubes (CNTs) have garnered extensive research interest in recent decades due to their exceptional intrinsic properties and potential applications including biomedicine [1,2], nanocomposites [3,4], electronics [5,6], optics [7,8], and sensing [9,10]. One of the main criteria for utilizing CNTs potential in full is the improvement of their dispersion and separation in nontoxic solvents. The entanglement or formation of CNT clusters due to Van der Waals forces and a large aspect ratio [11], poses the challenge for the dispersion of CNTs into a liquid to form a stable solution [12]. Significant efforts, including ball milling [13,14], high shear mixing [15], extrusion [16], high speed flow and high-pressure jet milling [17] have been made in the past decade to address the issue of CNT dispersion. Among them, ball milling demonstrates unique advantages, including: (i) the reduction in particle size of the milled CNTs, resulting in a more uniform distribution [18]; (ii) the high efficiencies in both energy utilization and dispersion compared to other techniques [19]. Yet, the length-to-diameter ratio of the milled CNTs has been significantly reduced [14], and the milling process tends to produce debris and other covalently bonded amorphous carbon species, such as oxygen-containing, nitrogen-containing, and other polar groups on the surface of the CNTs. This results in the contamination of

* Corresponding authors.
E-mail addresses: zhaosu@nimte.ac.cn (S. Zhao), barbara.maciejewska@materials.ox.ac.uk (B.M. Maciejewska), lqin1@uwyo.edu (L. Qin).

https://doi.org/10.1016/j.surfin.2024.104740
Received 9 April 2024; Received in revised form 29 June 2024; Accepted 3 July 2024
Available online 4 July 2024

CNTs [20,21].

Ultrasonic dispersion is another promising route to disperse CNTs with high deagglomeration capacity while maintaining the available length-to-diameter ratio [22]. The ultrasonic dispersion ability of CNTs is typically achieved through cavitation generation in the liquid medium. In the cavitation zone, ultrasonic bubbles can vibrate according to the alternating pressure, grow, coalescence and eventually collapse , creating a local shock wave with both high pressure and high temperature [23-25]. Such shockwave with high-speed micro jets is considered a crucial factor for breaking large CNT clusters into smaller fragments [26,27]. Moreover, the localized high-temperature and pressure resulting from bubble implosion within a sub-microsecond time scale can considerably accelerate the movement of CNT particles in the liquid, promoting the exfoliation and dispersion of the agglomerated CNTs [28, 29]. Additionally, periodically applied acoustic pressure can efficiently reduce the van der Waals force of CNTs, and the acoustic streaming flow can act as a macroscopic agitator to accelerate the diffusion of the dispersant [30]. However, achieving a high concentration CNTs solution through simply extending processing time remains challenging, given that CNT surfaces are hydrophobic. In this regard, several advanced methods have been proposed to enhanced the efficacy of CNT dispersion [31,32]. For example, the surfactants and milder sonication settings were employed to improve deagglomeration and reduce defects on CNTs during dispersion [33]. Cheng *et al.* dispersed single-walled CNTs (SWNTs) in various organic solvents using tip sonication and found that the aggregation fraction below the dispersion limit of SWNTs was influenced by the intrinsic parameters of the solvent, particularly its vapor pressure and viscosity[32]. Many of these studies involve the addition of organic surfactants to deionized water (DIW) or pure water [34] or the use of toxic organic solvents [32]. These methods often require an additional purification step, especially if removing the surfactant proves challenging [35,36]. Our previous work [37-40] has confirmed that DIW is an environmentally friendly liquid medium for exfoliating or dispersing nanomaterials under ultrasound. However, ultrasonic waves typically do not generate strong cavitation in DIW [39], resulting in a low yield (~5%) [41].

For several years our research has actively focused on the techniques of ultrasonic processing [36-40,42-44]. Here, we present a novel hydrostatic pressure-assisted ultrasound approach with the potential to scale up, aiming to achieve a high concentration and exceptionally stable dispersion of nanomaterials in DIW or other environmentally friendly solvents. To gain deeper insights into the underlying mechanism of ultrasonic dispersion of MWCNTs under hydrostatic pressure, we developed a numerical modeling to track the growth and collapse of ultrasonic bubbles during the dispersion process. Subsequently, the stability of the dispersion solvent was evaluated, and the nanobubbles (NBs) formed after bubble collapse under hydrostatic pressure were quantified. The contribution of NBs to the stability of their dispersions was elucidated. This study provides a practical method for fabricating a high-concentration MWCNTs dispersion solution, demonstrating significant potential for energy applications.

2. Materials and methods

2.1. Experimental apparatus design and measurement

The cyclic ultrasound-assisted dispersion apparatus was upgraded based on the previous design[39, 40]. Fig. 1a shows the 3D rendered schematic view of this apparatus. In this configuration, a needle valve was used to control the hydrostatic pressure within a range from 0 to 0.2 MPa in the chamber (Fig. 1a). The suspension temperature remained quasi-constant (40±5 °C) by controlling the flow rate of the external circulation water cooling system (Fig. 1c). An ultrasonic transducer system (ResoLabR-1500, Zhongke Leishun Intelligent Technology Co., Ltd.) equipped with a dumbbell probe was used to generate ultrasonic wave into the liquid. The measured frequency and the effective output power of the ultrasonic system was 20 kHz and 500 W, respectively. To understand the role of hydrostatic pressure in the cavitation evolution, real-time images were acquired during the sonication process. Several representative frames from imaging sequences of the cavitation zone

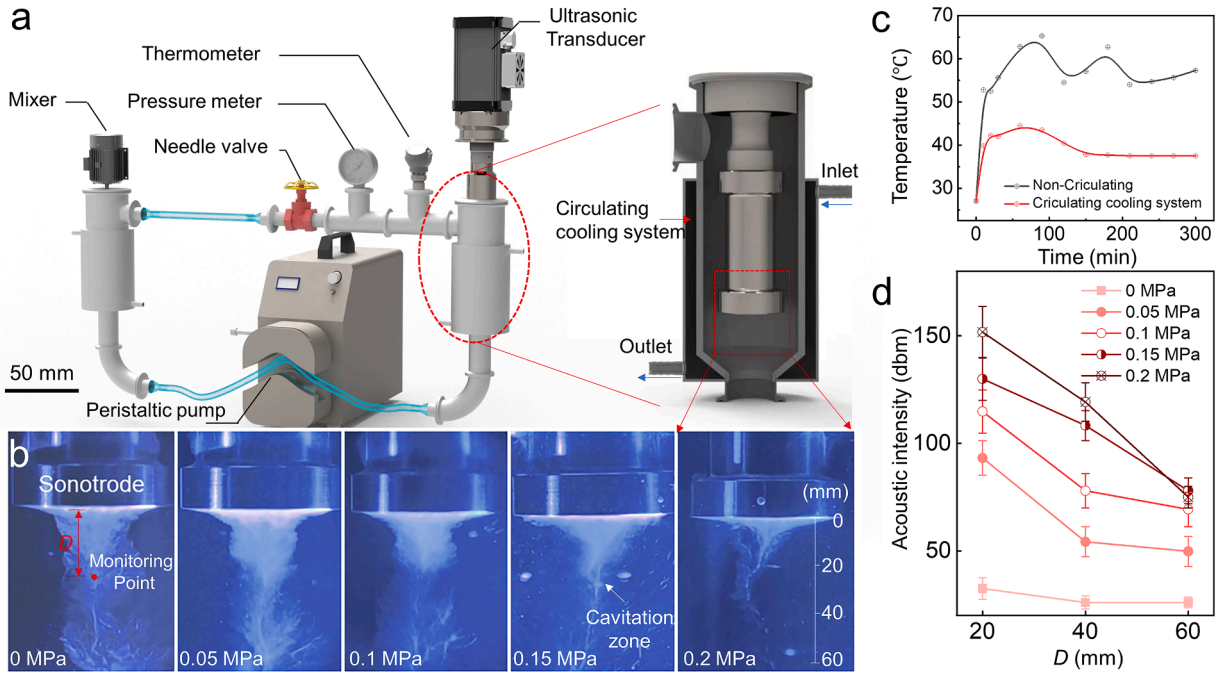

Fig. 1. (a) A CAD rendered scheme of the cyclic ultrasonic liquid phase dispersion apparatus, showing a combination of a hydrostatic pressure-controlled circulation system and a sonicator. To ensure the ultrasonic transducer operates in a suitable temperature environment, a constant-temperature cooling system was also integrated; (b) images captured by camera below sonotrode, showing the cavitation zone under various hydrostatic pressures in DIW; The specific locations of the monitors were marked in (b), where D represents the distance between the sonotrode tip and the sonic monitor. (c) temperature was measured by a K-type thermometer in (a). (d) the acoustic intensities under different hydrostatic pressures at distances (20, 40 and 60 mm) from sonotrode tip.

with different hydrostatic pressure were demonstrated in Fig. 1b. It is observed that the cavitation zone decreased as hydrostatic pressure increased in general. The acoustic intensity was measured by a sonic monitor (HUS-3 Portable Ultrasonic Sound Pressure Meter) located at different positions from the sonotrode tip (Fig. 1b). The acoustic intensity distribution analysis revealed that the increase of hydro-static pressures significantly boosts the acoustic intensity near the sonotrode tips where its attenuation is enhanced. As shown in Fig. 1d, the acoustic intensity is very similar for 0.15 MPa and 0.2 MPa at $D = 60$ mm.

2.2. Raw materials and sample preparation

MWCNTs obtained from Qingdao Chaorui Nano New Material Technology Co., Ltd., China, with an average diameter ranging from 5 to 12 nm and a length of ~50 μm, served as the raw material. A mixture of 1500 g of DIW, 15 g of MWCNTs, and 0.75 g of polyvinyl pyrrolidone (PVP) underwent preliminary stirring in the buffer tank for 3 h to achieve the initial suspension. Subsequently, ultrasound treatment was applied for a duration of 300 min. During this dispersion process, a cooling water system was employed to control the overall temperature at around 40±5 °C. To understand the dispersion process of MWCNTs and their stability in suspensions, a control experiment was conducted under atmospheric pressure (ATM) without added PVP, more detailed information can be found in the supplementary material.

2.3. Sample characterization and measurement

Samples were collected at half-hour intervals to enable real-time evaluations of viscosity and particle size. The particle dimensions of the MWCNTs and the viscosity of the dispersed suspension were determined using a laser particle size analyzer (Dandong Baxter) and a viscometer (U.S. Solid Model: USS-DVT4), respectively. The dispersed MWCNTs were characterised by means of scanning electron microscope (Hitachi S-4800) and transmission electron microscope (HRTEM-JEOL2100). The concentration of the solution was determined using a UV–Vis spectrophotometer (Lambda 1050), and measurement wavelength range of 220 to 1200 nm (Specific details are in supplementary materials). For UV characterization, the CNTs dispersion underwent a 200-fold dilution with DI water and was subsequently centrifuged at 45,000 g for 30 min. The scanning speed during UV analysis was set at 400 nm/min. Baseline correction was conducted using 10 mm quartz cuvettes and DI water. Raman spectra were recorded using a Renishaw inVia Raman instrument with a 532 nm laser (2.33 eV) at an intensity of 10%. To ensure reliability, Raman spectra were collected from at least 20 random positions within the range of 1000 to 3200 cm^{-1}.

To evaluate the size distribution, concentration and zeta potential of bubble solution under different hydrostatic pressures, ZetaView Nanoparticle Tracking Analysis (NTA) and Zetasizer (DLS) were employed. Liquid cell was considered a complementary method for visualizing NBs using Tecnai F20 TEM and liquid cell. X-ray images were acquired using an instrument with an operating voltage of 5 kV.

To prepare buckypaper using a vacuum filtration setup, 50 g of the dispersed CNTs solution (with a CNT solid content of 1%), subjected to ultrasonic treatment for 300 min, was placed into a beaker. Using a dropper, 2–5 ml of the sample was extracted and filtered through a 0.45 μm PTFE filter membrane for approximately 1 hour. After filtration, the filter membrane was allowed to dry naturally. Subsequently, the buckypaper was carefully peeled off the filter membrane, and its resistance and thickness were measured using Van Der Pauw (VDP) method.

3. Results and discussion

3.1. MWCNTs characterization after dispersion

The UV–vis evaluation (see Fig. S1 in Supplementary materials) of the dispersed MWCNT solutions under hydrostatic pressure reveals the higher concentration compared to those produced under ATM (Fig. 2f). In particular, the concentration of the dispersed MWCNT solution at 0.1 MPa presents the maximum value of ~4.23 mg/ml, more than two-fold of that achieved under ATM. To investigate the impact of ultrasonic duration on the dispersion level, the treatment time was extended from 300 min to 540 min under ATM. As shown in Fig. S3, the particle size decreased from 37.3 μm to 23.6 μm after 300 min of ultrasonic treatment. However, even when the sonication time was extended to 540 min, the particle size range did not decrease further. In contrast, under a hydrostatic pressure of 0.1 MPa, the particle size continued to decrease from 38.4 μm to 7.2 μm. Therefore, we suggest that the hydrostatic pressure is considered the dominant factor in achieving a good dispersion of MWCNTs.

The electrical conductivity of the buckypaper was evaluated through four-probe measurements, as schematically shown in Fig. 2e. The buckypaper peeled off from the PTFE film is shown in Fig. 2a&b. The thickness of the buckypaper ranges from 0.7 to 1.6 μm. The average electrical resistivity was calculated using the Van Der Pauw (VDP) method[45]. The electrical conductivity of the buckypaper made from MWCNTs dispersed under a hydrostatic pressure of 0.1 MPa is ~4938 S/m in Fig. 2f, which exceeds the conductivities reported in previous studies [46–50] in Table 1. Such enhanced conductivity can be attributed to the improved dispersion of MWCNTs on the surface of the film, leading to a reduction in the number of interconnections between MWCNTs per unit area. CNTs possess high conductivity and a high aspect ratio, facilitating the formation of a network of conductive tubes from buckypaper. The ideal structure of buckypapers should have all the CNTs connected with others to form a network structure. Poor dispersion often leads to significant agglomeration, thereby increasing the number of contact points per unit area in the network and consequently raising resistance. Conversely, over-dispersion can compromise the aspect ratio of CNTs, also resulting in an increase in contact points per unit area. In our study, under ATM, visible agglomeration phenomena are often observed from backypaper in Fig. S5. In contrast, at a hydrostatic pressure of 0.2 MPa, although good dispersion can be achieved, simulation results show that the implosion of bubbles after two cycles releases shockwaves with a peak pressure value as high as 62 MPa. Under such intense shockwaves, MWCNTs can be effectively fragmented, leading to a sharp drop in aspect ratio. At 0.1 MPa, not only is the agglomeration phenomenon largely eliminated, but the aspect ratio of MWCNTs is also maintained to a certain extent.

Raman spectra of the dispersed MWCNTs under various hydrostatic pressure show three distinctive peaks at 1350 cm^{-1}, 2750 cm^{-1} and 1590 cm^{-1} for all samples, corresponding to D band, 2D band and G band, respectively [51]. A profile of the ID/IG ratio was plotted as a function of applied hydrostatic pressure in Fig. S2, as the raw materials have the lowest I_D/I_G value of 0.3. In contrast, the ID/IG ratio increases from 0.41 up to 0.46 with increasing hydrostatic pressure, indicating that more surface defects are generated as the hydrostatic pressure increases.

3.2. Real-time measurement and stability assessment

For assessing the dispersion dynamics of the ultrasonicated MWCNT solution, real-time measurements of MWCNT particle size and solution viscosity with PVP were conducted (Fig. 3a&3b), revealing three distinct stages in their evolution. In stage I (0–60 mins), the particle size decreases rapidly, with a slight increase in the suspension viscosity. Stage II corresponds to 60–180 mins, during which the viscosity of the suspension significantly increases from 300 to 3400 mPa.s, while the particle size reduction is no longer relevant. In Stage III (>180 mins), the particle size remains unchanged, while the viscosity of the suspension decreases. Detailed measurement data without PVP are shown in Fig. S4.

3.3. Ultrasonic bubble dynamics

The ultrasonication driven dispersion process is primarily initiated

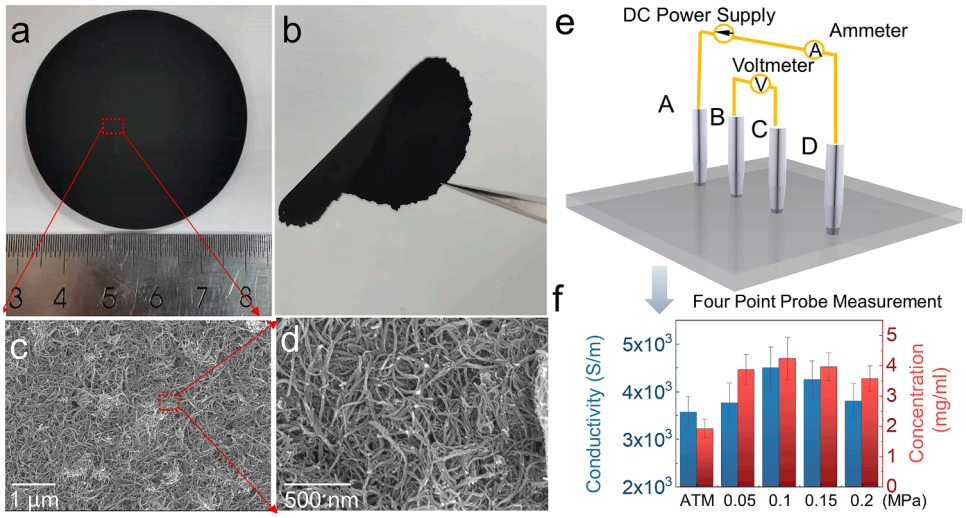

Fig. 2. (a) and (b) Photos of buckypaper prepared under a hydrostatic pressure of 0.1 MPa; (c) and (d) SEM images showing the top surface of the buckypaper; (e) schematic diagram illustrating the four-point method used to measure the thin film electrical conductivity; (f) the hydrostatic pressure dependence of the electrical conductivity of buckypaper and concentration of the dispersed MWCNTs, indicating that the dispersed CNTs solution and buckypaper exhibit the highest concentration (~4.23 mg/ml) and electrical conductivity (~4938 S/m) when ultrasonicated at 0.1 MPa, respectively.

Table 1
Electrical conductivity of Bucky paper produced via sonication in relation to duration time and media.

No.	Method	Materials	Dispersion Medium	Time (h)	Electrical Conductivity (S/m)	Refs.
1	Bath-sonication	MWCNTs	HNO_3	1	700	[46]
2	Tip-sonication	MWCNTs	PAN solution	3	1000	[47]
3	Bath-sonication	MWCNTs	H_2SO_4 (98%)/HNO_3 (70%)	3	1000	[48]
4	Tip- sonication	MWCNTs	Aqueous solution	1	3300	[49]
5	Jet-milling	SWCNT s	methyl isobutyl ketone (MIBK)	–	4500	[50]
6	Hydrostatic Pressure Assisted Ultrasound	MWCNTs	DI Water	5	4230	This work
7	Hydrostatic Pressure Assisted Ultrasound	MWCNTs	DI Water+PVP	5	4938	This work

by shockwaves induced by bubble implosion shockwave induced by bubble implosion [37]. To understand bubble dynamics in DIW under hydrostatic pressures, we conducted multiphysics modeling as described in detail in our previous work [43].Fig. 4a &b depicts the dynamics of a single bubble and the velocity vector below the sonotrode tip during an acoustic cycle. The pressure distribution is shown on the left side of the bubble morphology. The modeling results indicate that four typical stages occur during ultrasonic treatment, namely, the bubble compression (Fig. 4b1-b3), the formation of a C-shape configuration (Fig. 4b4) at top surface of the bubbles, and the bubble disintegration (Fig. 4b5&6). The shockwave (Fig. 4a) occurs at the top of the bubble as the bubble forms a C-shape configuration and immediately spreads outward. The pressure profiles of the bubble over time at a distance of 1 μm were tracked in order to better evaluate the shock strength and features under different conditions. In our previous work, we showed that the shockwave released by the bubble implosion can reach up to 1.6 MPa in DIW at atmosphere [43]. Herein, the peak value of the shock wave (illustrated by the green line) reaches 15 MPa under a hydrostatic pressure of 0.1 MPa (see Fig. 4e). This increase significantly enhances the energy released during the bubble implosion. Such improvement of hydrostatic pressure-induced bubble implosion is in line with earlier experimental findings [52].

To understand the significant viscosity increase in stages II and III of Fig. 4b, two cases were examined. In the reference case of 0.1 MPa, the pressure of the shockwave in a solution with 1580 mPa.s viscosity value was about 6.8 MPa, much lower than that in DIW (15 MPa) as shown in Fig. 4d. However, with increasing viscosity, the shockwave intensity was attenuated. In another case at 0.2 MPa hydrostatic pressure with the same viscosity, the bubble imploded after two cycles and released shockwaves with a pressure peak value as high as 62 MPa. After the first-round shockwave, the shockwave can be continuously produced over the next ten cycles. Additionally, the shockwave intensity increased with solution viscosity, as shown in Fig. 4e. After just 4 cycles, the shockwave intensity reached 80 MPa for the solution with a viscosity of 3226 mPa.s. The simulation results show a critical acoustic pressure (P_{crit}) for the viscosity solution in this study. Exceeding this pressure threshold leads to bubble implosion, generating a high-intensity and high-frequency shockwave. On the contrary, the shockwave could be dissipated due to the nature of viscous fluids. To fully understand the interaction between imploding bubbles and the surface of MWCNTs, a bubble-fluid-structure coupled numerical simulation was carried based on our previous modeling [37,43].

Fig. 4c shows that the shear stresses at the surface of MWCNTs induced by bubble implosion. The shear stress level in viscous fluid reached 20~25 MPa, much higher than that in DIW (~8 MPa), which may lead to the direct fracture of MWCNTs within a few microseconds. In stage I (0–60 mins), the introduction of hydrostatic pressure environment enhances the shockwave since the solution was non-viscous fluid (1 mPa.s) and the fragmentation induced by cavitation bubble implosion plays a major role to disperse the MWCNTs. The suspension viscosity greatly increased up to ~3400 mPa.s in Stage II. Therefore, two situations can be expected. As the pressure threshold has not reached, the energy released by the bubble implosion weakens and thus the micro jet induced by the bubbles plays a more role in deagglomeration, as in the case of 0.1 MPa. Once the pressure exceeds the threshold value, the shockwave released by the bubbles is boosted to more than 3 times the initial pressure, which makes the MWCNTs further fragmentation, and the aspect ratio of MWCNTs was greatly reduced, as in the case of 0.2 MPa.

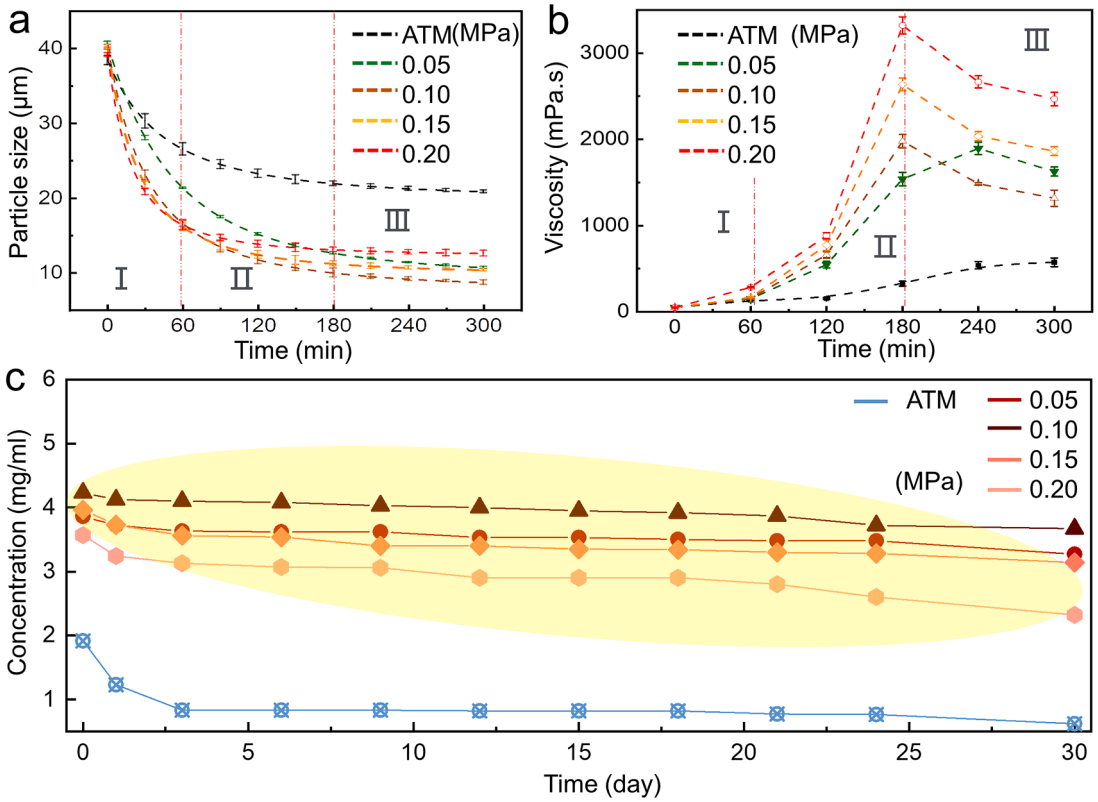

Fig. 3. Evolution of (a) the particle size of the dispersed MWCNTs and (b) solution viscosity as a function of ultrasound time under different hydrostatic pressures. Three stages are distinguished: I: MWCNTs fragmentation by ultrasonic bubble, II: MWCNTs dispersed by ultrasonic bubble, III: MWCNTs dispersed by acoustic swirling flow. (c) The long-term stability of MWCNT solutions sonicated at hydrostatic pressures ranging from 0 to 0.2 MPa is presented, highlighting the exceptional stability of the dispersion achieved under hydrostatic pressure compared to ATM.

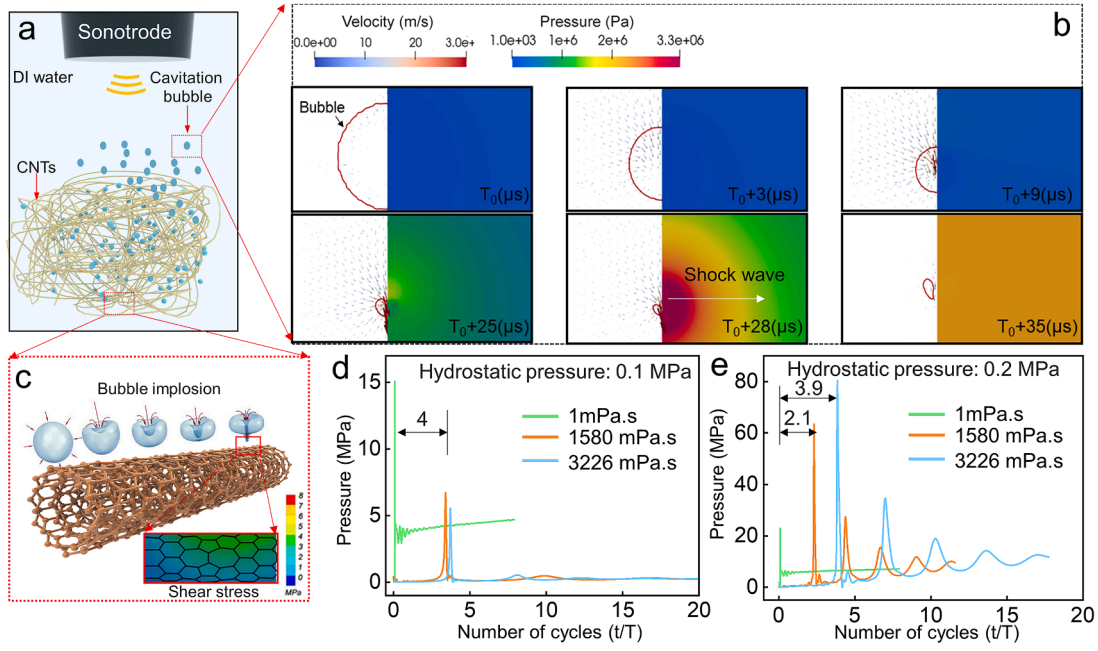

Fig. 4. (a) Schematic diagram of bubbles landed onto bundled MWCNTs; (b) the simulated sequences of the process of individual bubble compression by acoustic pressure and following implosion in an acoustic cycle (Left: bubble morphology and velocity vector, Right: the pressure distribution); (c) schematic illustration of bubble implosion acting on carbon nanotubes, insert shows the shear stress distribution on carbon nanotubes as the bubble implodes at hydrostatic pressures of 0.2 MPa and the pressure profiles at different viscosities as the bubble implodes at hydrostatic pressures of (b) 0.1 MPa and (c) 0.2 MPa.

3.4. Ultrasonic nanobubble under hydrostatic pressure

After ultrasonic dispersion, we used DIW to analyze the concentration and distribution of bubbles in the solution. Our findings confirm that ultrasound creates a stable cavitation zone below the probe, filled with visible microbubbles (MBs), and triggers the notable presence of MBs but also triggers a notable presence of NBs within the solution due to bubble fragmentation from implosion. Notably, at a hydrostatic pressure of 0.15 MPa, the concentration of NBs escalates to as high as 9.2e+6 bubbles/ml. Under atmospheric pressure, bubbles predominantly exist in the micron scale, and the concentration of nanobubbles is minimal. However, when the hydrostatic pressure increases to 0.15 MPa, there is a significant increase in the concentration of NBs, rising from 2×10^5 to 9×10^6 bubbles/ml, as depicted in Fig. 5c. Beyond the 0.15 MPa threshold, there is a decrease in the number of NBs, and an increase in the number of microbubbles. A similar trend is observed in the zeta potential of the solution as shown in Fig. 5d, indicating a decline in the dispersion stability of the solution.

Previous research has indicated that the transition of bubbles from nanoscale to micron scale occurs with increasing hydrostatic pressure through two main mechanisms: 1) growth of NBs[53] or 2 fusion or merging of multiple NBs [53]. To understand the underlying reasons, the bubble solution was examined, revealing that the observed large MBs are clusters formed by the aggregation of smaller-scale NBs (Fig. 5f). In classical cavitation theory, the generation of NBs in an acoustic field is linked to the collapse of cavitation microbubbles [54]. Increased concentration of nuclei (dissolved gas molecules) or longer sonication time results in higher frequency of transient cavitation events, leading to the formation of more NBs. In our study, the source of negative ions is most likely attributed to the presence of NBs induced by the collapse of ultrasonic bubbles [53,55]. Numerous experiments have shown that bulk NBs in liquid media are often characterized by a high magnitude of zeta potential and negatively charged surface [54]. Under hydrostatic pressure conditions, the collapse of ultrasonic bubbles is intensified due to the increased hydrostatic pressure and viscosity of the solution, as shown in our simulation results in Fig. 4d&4e. This phenomenon leads to the generation of a greater number of negatively charged NBs and ions. The dispersed solution maintains remarkable stability due to two primary factors. Firstly, the substantial specific surface area of NBs enables effective adsorption on dispersed CNTs. Secondly, negatively charged ions, such as OH− and HCO3−, generated by NBs, exhibit elevated adsorption energy on the hydrophobic interface. As a result, the CNTs surface selectively attracts these negatively charged ions, causing H+ ions to remain in the DI water, leading to a negatively charged gas-liquid interface on the CNTs surface.

4. Conclusions

This study developed a cyclic apparatus for systematically investigating the effect of hydrostatic pressure on MWCNTs ultrasonic dispersion in DI water. Real-time acoustic examination and modeling quantified the cavitation zone and acoustic intensity under hydrostatic pressure conditions. The beneficial effect of hydrostatic pressure on dispersion is primarily attributed to enhanced shock waves, resulting from ultrasonic bubbles implosion. Using MWCNTs as a case study, we quantitatively examined changes in solution properties during the dispersion process, particularly the transition from a non-viscous to a highly viscous fluid. The study showed that the shock wave intensity in viscous fluids can be effectively regulated by external hydrostatic pressure. Numerical model estimates showed a fivefold increase in shock wave intensity with external hydrostatic pressure above the threshold, significantly enhancing the fragmentation efficiency. The hydrostatic pressure environment also promotes the generation of NBs contributing to maintaining excellent solution stability. Our hydrostatic pressure-

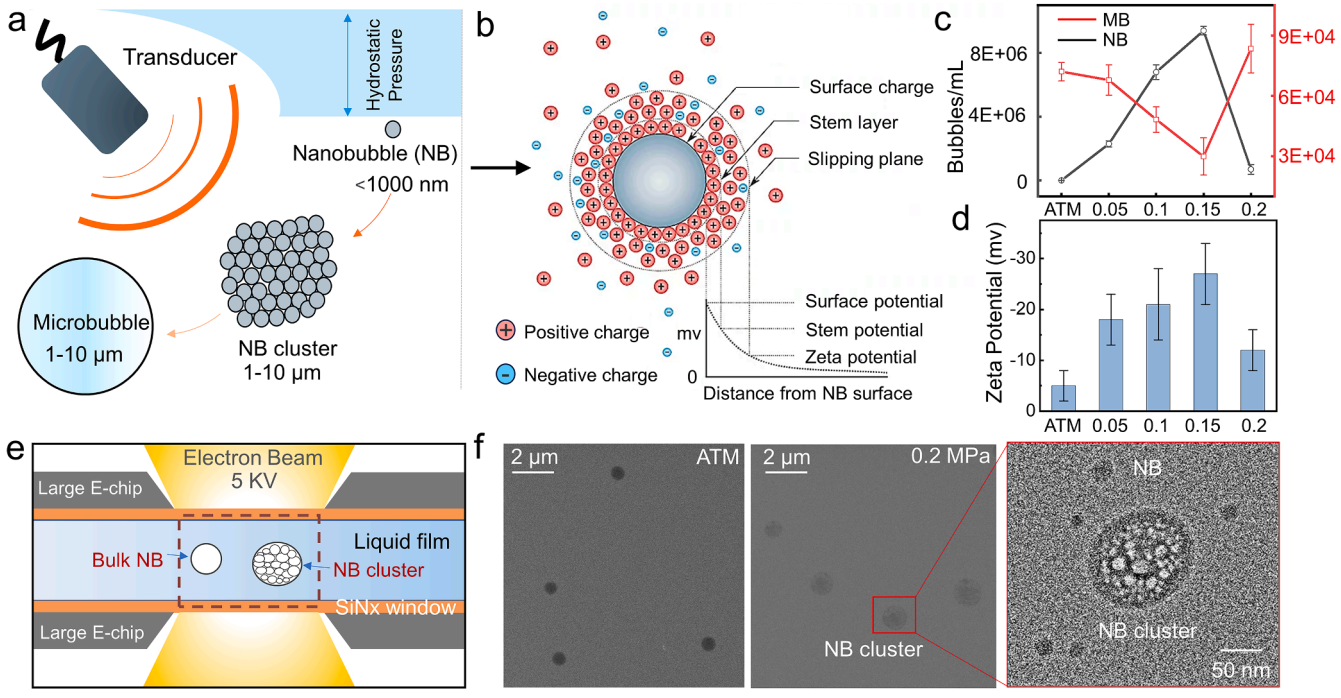

Fig. 5. (a) The schematic diagram illustrates that under atmospheric pressure (atm), acoustic pressure can trigger micron-scale bubbles (MBs). It's interesting to note that hydrostatic pressure applied promotes the formation of NBs, which can then cluster together under certain conditions; (b) the electronic structure of NBs, which differs from MB in long-term stable features due to the charge distribution on their perimeter; (c) Concentrations of MBs and NBs, and (d) Zeta potential in DI water under different pressure conditions. (e) for imaging analysis, the NBs solution was stored in a liquid cell. The chamber comprised a micro-channel and a membrane, with the chip placed at the center of the micro-channel substrate. A 1 mL solution of NBs was drawn up to the chip surface. Finally, the lid was placed on the holder and twisted slightly. The x-ray images were recorded by an instrument operated at an accelerating voltage of 5 kV. (f) At ATM pressure and a hydrostatic pressure of 0.2 MPa, respectively, individual NB and a few NB clusters were observed.

assisted ultrasonic dispersion approaches are applicable for dispersing various nanomaterials.

CRediT authorship contribution statement

Lei Yu: Investigation, Funding acquisition, Data curation. **Yibiao Lin:** Investigation, Formal analysis, Data curation. **Lianxia Li:** Software, Investigation. **Hu Zong:** Investigation. **Ying Zhou:** Funding acquisition. **Su Zhao:** Funding acquisition. **Zhiguo Zhang:** Writing – review & editing. **Nicole Grobert:** Writing – review & editing, Supervision. **Barbara M Maciejewska:** Writing – review & editing, Investigation. **Ling Qin:** Writing – review & editing, Writing – original draft, Software, Investigation, Data curation, Methodology, Validation, Visualization.

Declaration of competing interest

The authors declare that they have no known competing financial interests or personal relationships that could have appeared to influence the work reported in this paper.

Data availability

Data will be made available on request.

Acknowledgements

The authors would like to acknowledge the financial support from the Ningbo Key Projects of Science and Technology Innovation 2025 Plan (2022Z043), Innovation 2025 Major Special Project (2022Z68), Ningbo Natural Science Foundation (2021J221) and Natural Science Basic Research Program of Shaanxi (Program No. 2021JM-402). Additionally, the authors thank Dr. Zhian Deng for his contribution to the discussion section of the revised manuscript.

Supplementary materials

Supplementary material associated with this article can be found, in the online version, at doi:10.1016/j.surfin.2024.104740.

References

[1] N. Sinha, J.-W. Yeow, Carbon nanotubes for biomedical applications, IEEE Trans. Nanobiosci. 4 (2) (2005) 180–195.
[2] W. Yang, P. Thordarson, J.J. Gooding, S.P. Ringer, F. Braet, Carbon nanotubes for biological and biomedical applications, Nanotechnology 18 (41) (2007) 412001.
[3] Y.S. Song, J.R. Youn, Influence of dispersion states of carbon nanotubes on physical properties of epoxy nanocomposites, Carbon 43 (7) (2005) 1378–1385.
[4] P.-C. Ma, N.A. Siddiqui, G. Marom, J.-K. Kim, Dispersion and functionalization of carbon nanotubes for polymer-based nanocomposites: a review, Compos. Part A 41 (10) (2010) 1345–1367.
[5] D. Li, W.Y. Lai, Y.Z. Zhang, W. Huang, Printable transparent conductive films for flexible electronics, Adv. Mater. 30 (10) (2018) 1704738.
[6] W. Jayathilaka, A. Chinnappan, S. Ramakrishna, A review of properties influencing the conductivity of CNT/Cu composites and their applications in wearable/flexible electronics, J. Mater. Chem. C 5 (36) (2017) 9209–9237.
[7] X. Wei, S. Li, W. Wang, X. Zhang, W. Zhou, S. Xie, H. Liu, Recent advances in structure separation of single-wall carbon nanotubes and their application in optics, electronics, and optoelectronics, Adv. Sci. 9 (14) (2022) 2200054.
[8] H.M. Alghamdi, A. Rajeh, Synthesis of carbon nanotubes/titanium dioxide and study of its effect on the optical, dielectric, and mechanical properties of polyvinyl alcohol/sodium alginate for energy storage devices, Int. J. Energy Res. 46 (14) (2022) 20050–20066.
[9] Q. Duan, B. Lan, Y. Lv, Highly dispersed, adhesive carbon nanotube ink for strain and pressure sensors, ACS Appl. Mater. Interfaces 14 (1) (2022) 1973–1982.
[10] H. Beitollahi, F. Movahedifar, S. Tajik, S. Jahani, A review on the effects of introducing CNTs in the modification process of electrochemical sensors, Electroanalysis 31 (7) (2019) 1195–1203.
[11] L. Qiao, K. Du, Scalable production of high-quality carbon nanotube dispersion in aqueous solution using cellulose as dispersant by a freezing/thawing process, J. Colloid. Interface Sci. 623 (2022) 1200–1209.
[12] B.M. Maciejewska, L.E. Coy, K.K. Koziol, S. Jurga, Facile synthesis of highly stable and water-soluble magnetic MWCNT/α-Fe nanocomposites, J. Phys. Chem. C 118 (48) (2014) 27861–27869.
[13] D. Jayaraman, Effect of high energy ball milling on reinforcement of MWCNTs in magnesium nano composites, Int. J. Adv. Sci. Technol 29 (2020) 4174–4179.
[14] B. Krause, T. Villmow, R. Boldt, M. Mende, G. Petzold, P. Pötschke, Influence of dry grinding in a ball mill on the length of multiwalled carbon nanotubes and their dispersion and percolation behaviour in melt mixed polycarbonate composites, Compos. Sci. Technol. 71 (8) (2011) 1145–1153.
[15] T. Panagiotou, J.M. Bernard, S.V. Mesite, Deagglomeration and dispersion of carbon nanotubes using microfluidizer high shear fluid processors, in: Nano Science and Technology Institute (NSTI) Conference and Expo Proceedings, 2008, pp. 39–42.
[16] T. Yokozeki, Y. Iwahori, M. Ishibashi, T. Yanagisawa, K. Imai, M. Arai, T. Takahashi, K. Enomoto, Fracture toughness improvement of CFRP laminates by dispersion of cup-stacked carbon nanotubes, Compos. Sci. Technol. 69 (14) (2009) 2268–2273.
[17] H. Yoon, M. Yamashita, S. Ata, D.N. Futaba, T. Yamada, K. Hata, Controlling exfoliation in order to minimize damage during dispersion of long SWCNTs for advanced composites, Sci. Rep. 4 (1) (2014) 3907.
[18] N. Darsono, D.-H. Yoon, J. Kim, Milling and dispersion of multi-walled carbon nanotubes in texanol, Appl. Surf. Sci. 254 (11) (2008) 3412–3419.
[19] J. Song, W. Chen, L. Dong, J. Wang, N. Deng, An electroless plating and planetary ball milling process for mechanical properties enhancement of bulk CNTs/Cu composites, J. Alloys. Compd. 720 (2017) 54–62.
[20] G. Gorrasi, M. Sarno, A. Di Bartolomeo, D. Sannino, P. Ciambelli, V. Vittoria, Incorporation of carbon nanotubes into polyethylene by high energy ball milling: morphology and physical properties, J. Polym. Sci. Part B 45 (5) (2007) 597–606.
[21] C. Vishal, S.K. Raju Chinthalapati, R. Krishna Kanala, R. Raman, R. Rao Bojja, R. Kanaparthi, Effect of ball milling and oxidation on dispersibility and dispersion stability of multiwalled carbon nanotubes in high viscous heat exchange fluids, ChemistrySelect 5 (23) (2020) 7031–7039.
[22] S. Bahrani, M. Ghaedi, M.J.K. Mansoorkhani, A. Asfaram, A.A. Bazrafshan, M. K. Purkait, Ultrasonic assisted dispersive solid-phase microextraction of Eriochrome Cyanine R from water sample on ultrasonically synthesized lead (II) dioxide nanoparticles loaded on activated carbon: experimental design methodology, Ultrason. Sonochem. 34 (2017) 317–324.
[23] B. Wang, D. Tan, T.L. Lee, J.C. Khong, F. Wang, D. Eskin, T. Connolley, K. Fezzaa, J. Mi, Ultrafast synchrotron X-ray imaging studies of microstructure fragmentation in solidification under ultrasound, Acta Mater. 144 (2018) 505–515.
[24] B.E. Noltingk, E.A. Neppiras, Cavitation produced by ultrasonics, Proc. Phys. Soc. Section B 63 (9) (1950) 674.
[25] J. Rooze, E.V. Rebrov, J.C. Schouten, J.T. Keurentjes, Dissolved gas and ultrasonic cavitation–a review, Ultrason. Sonochem. 20 (1) (2013) 1–11.
[26] S. Wang, J. Kang, X. Zhang, Z. Guo, Dendrites fragmentation induced by oscillating cavitation bubbles in ultrasound field, Ultrasonics 83 (2018) 26–32.
[27] Z. Zhang, C. Wang, B. Koe, C.M. Schlepütz, S. Irvine, J. Mi, Synchrotron X-ray imaging and ultrafast tomography in situ study of the fragmentation and growth dynamics of dendritic microstructures in solidification under ultrasound, Acta Mater. 209 (2021) 116796.
[28] S. Li, R. Han, A. Zhang, Nonlinear interaction between a gas bubble and a suspended sphere, J. Fluids. Struct. 65 (2016) 333–354.
[29] I. Tzanakis, D. Eskin, A. Georgoulas, D. Fytanidis, Incubation pit analysis and calculation of the hydrodynamic impact pressure from the implosion of an acoustic cavitation bubble, Ultrason. Sonochem. 21 (2) (2014) 866–878.
[30] M.S. Strano, V.C. Moore, M.K. Miller, M.J. Allen, E.H. Haroz, C. Kittrell, R. H. Hauge, R. Smalley, The role of surfactant adsorption during ultrasonication in the dispersion of single-walled carbon nanotubes, J. Nanosci. Nanotechnol. 3 (1–2) (2003) 81–86.
[31] W.R. Jung, J.H. Choi, N. Lee, K. Shin, J.-H. Moon, Y.-S. Seo, Reduced damage to carbon nanotubes during ultrasound-assisted dispersion as a result of supercritical-fluid treatment, Carbon 50 (2) (2012) 633–636.
[32] Q. Cheng, S. Debnath, E. Gregan, H.J. Byrne, Ultrasound-assisted SWNTs dispersion: effects of sonication parameters and solvent properties, J. Phys. Chem. C 114 (19) (2010) 8821–8827.
[33] J.I. Paredes, M. Burghard, Dispersions of individual single-walled carbon nanotubes of high length, Langmuir 20 (12) (2004) 5149–5152.
[34] J.N. Coleman, Liquid exfoliation of defect-free graphene, Acc. Chem. Res. 46 (1) (2013) 14–22.
[35] A.V. Tyurnina, J.A. Morton, T. Subroto, M. Khavari, B. Maciejewska, J. Mi, N. Grobert, K. Porfyrakis, I. Tzanakis, D.G. Eskin, Environment friendly dual-frequency ultrasonic exfoliation of few-layer graphene, Carbon 185 (2021) 536–545.
[36] K.L. Ng, B.M. Maciejewska, L. Qin, C. Johnston, J. Barrio, M.-M. Titirici, I. Tzanakis, D.G. Eskin, K. Porfyrakis, J. Mi, Direct evidence of the exfoliation efficiency and graphene dispersibility of green solvents toward sustainable graphene production, ACS Sustain. Chem. Eng. 11 (1) (2022) 58–66.
[37] L. Qin, B.M. Maciejewska, T. Subroto, J.A. Morton, K. Porfyrakis, I. Tzanakis, D. G. Eskin, N. Grobert, K. Fezzaa, J. Mi, Ultrafast synchrotron X-ray imaging and multiphysics modelling of liquid phase fatigue exfoliation of graphite under ultrasound, Carbon 186 (2022) 227–237.
[38] J.A. Morton, M. Khavari, L. Qin, B.M. Maciejewska, A.V. Tyurnina, N. Grobert, D. G. Eskin, J. Mi, K. Porfyrakis, P. Prentice, New insights into sono-exfoliation mechanisms of graphite: in situ high-speed imaging studies and acoustic measurements, Mater. Today 49 (2021) 10–22.

[39] M. Gao, H. Zong, Y. Li, Y. Zhou, L. Yu, L. Qin, S. Zhao, Novel cyclic ultrasound-assisted liquid phase exfoliation of graphene in deionized water: a parameter study, Mater. Lett. 337 (2023) 134011.
[40] Y. Weng, L. Li, S. Jiang, L. Qin, Y. Zhu, Nanobubble-assisted liquid phase exfoliation of graphene in deionized water, Mater. Lett. 364 (2024) 136372.
[41] A.V. Tyurnina, J.A. Morton, A. Kaur, J. Mi, N. Grobert, K. Porfyrakis, I. Tzanakis, D. G. Eskin, Effects of green solvents and surfactants on the characteristics of few-layer graphene produced by dual-frequency ultrasonic liquid phase exfoliation technique, Carbon 206 (2023) 7–15.
[42] H. Huang, L. Qin, H. Tang, D. Shu, W. Yan, B. Sun, J. Mi, Ultrasound cavitation induced nucleation in metal solidification: an analytical model and validation by real-time experiments, Ultrason. Sonochem. 80 (2021) 105832.
[43] L. Qin, K. Porfyrakis, I. Tzanakis, N. Grobert, D.G. Eskin, K. Fezzaa, J. Mi, Multiscale interactions of liquid, bubbles and solid phases in ultrasonic fields revealed by multiphysics modelling and ultrafast X-ray imaging, Ultrason. Sonochem. 89 (2022) 106158.
[44] A. Priyadarshi, S.B. Shahrani, T. Choma, L. Zrodowski, L. Qin, C.L.A. Leung, S. J. Clark, K. Fezzaa, J. Mi, P.D. Lee, New insights into the mechanism of ultrasonic atomization for the production of metal powders in additive manufacturing, Addit. Manuf. 83 (2024) 104033.
[45] S.K. Pandey, A. Manivannan, A fully automated temperature-dependent resistance measurement setup using van der Pauw method, Rev. Sci. Instrum. 89 (3) (2018).
[46] L. Cao, Y. Liu, J. Wang, Y. Pan, Y. Zhang, N. Wang, J. Chen, Multi-functional properties of MWCNT/PVA buckypapers fabricated by vacuum filtration combined with hot press: thermal, electrical and electromagnetic shielding, Nanomaterials 10 (12) (2020) 2503.
[47] Y. Kwon, W. Shim, S.-Y. Jeon, J.-H. Youk, W.-R. Yu, Improving dispersion of multi-walled carbon nanotubes and graphene using a common non-covalent modifier, Carbon Lett. 20 (2016) 53–61.
[48] M.J. Yee, N. Mubarak, M. Khalid, E. Abdullah, P. Jagadish, Synthesis of polyvinyl alcohol (PVA) infiltrated MWCNTs buckypaper for strain sensing application, Sci. Rep. 8 (1) (2018) 1–16.
[49] S. Lu, J. Shao, K. Ma, X. Wang, L. Zhang, Q. Meng, Fabrication of single/multi-walled hybrid buckypaper composites and their enhancement of electromagnetic interference shielding performance, J. Phys. D 49 (44) (2016) 445308.
[50] S. Sakurai, F. Kamada, D.N. Futaba, M. Yumura, K. Hata, Influence of lengths of millimeter-scale single-walled carbon nanotube on electrical and mechanical properties of buckypaper, Nanoscale Res. Lett. 8 (1) (2013) 546.
[51] C. Herrero-Latorre, J. Álvarez-Méndez, J. Barciela-García, S. García-Martín, R. Peña-Crecente, Characterization of carbon nanotubes and analytical methods for their determination in environmental and biological samples: a review, Anal. Chim. Acta 853 (2015) 77–94.
[52] C. Sauter, M. Emin, H. Schuchmann, S. Tavman, Influence of hydrostatic pressure and sound amplitude on the ultrasound induced dispersion and de-agglomeration of nanoparticles, Ultrason. Sonochem. 15 (4) (2008) 517–523.
[53] A.J. Jadhav, M. Barigou, On the clustering of bulk nanobubbles and their colloidal stability, J. Colloid. Interface Sci. 601 (2021) 816–824.
[54] X. Bu, M. Alheshibri, The effect of ultrasound on bulk and surface nanobubbles: a review of the current status, Ultrason. Sonochem. 76 (2021) 105629.
[55] D. Shin, J.B. Park, Y.-J. Kim, S.J. Kim, J.H. Kang, B. Lee, S.-P. Cho, B.H. Hong, K. S. Novoselov, Growth dynamics and gas transport mechanism of nanobubbles in graphene liquid cells, Nat. Commun. 6 (1) (2015) 6068.